Numerical modelling of surface roughness effect on the fatigue behavior of Ti-6Al-4V obtained by additive manufacturing

Bastien Vayssette, Nicolas Saintier, Charles Brugger, Mohamed El May, Etienne Pessard

ELSEVIER

Available online at www.sciencedirect.com

ScienceDirect

International Journal of Fatigue 00 (2019) 1–31

Journal Logo

www.elsevier.com/locate/procedia

International Journal of Fatigue

Numerical modelling of surface roughness effect on the fatigue behavior of Ti-6Al-4V obtained by additive manufacturing

Bastien Vayssette[a], Nicolas Saintier[a], Charles Brugger[a], Mohamed El May[a], Etienne Pessard[b]

[a]*Arts et Metiers Paristech, I2M, CNRS, Talence 33400, France*
[b]*Arts et Metiers Paristech, LAMPA, Angers 49035, France*

Abstract

Selective Laser Melting (SLM) is a powder bed fusion process which allows to build-up parts by successive addition of layers using 3D-CAD models. Among the advantages, the high degree of freedom for part design and the small loss of material explain the increasing number of Ti-6Al-4V parts obtained by this process. However, right after additive manufacturing, these parts contain defects (surface roughness, porosity, residual stresses) which significantly decrease the High Cycle Fatigue (HCF) life. In order to minimize the porosity and residual stresses, post-processing treatments like Hot Isostatic Pressing (HIP) and Stress Relieving (SR) are often conducted. But the reduction of the surface roughness by machining is very costly and not always possible, especially for parts with complex geometry. The aim of this work is to evaluate the effect of the surface roughness of Ti-6Al-4V parts produced by SLM on the HCF behavior and to propose a methodology to estimate this effect. Three sets of specimens were tested in tension-compression: Hot-Rolled (reference) ; SLM HIP machined ; SLM HIP as-built. For each condition, microstructure characterization, observation of the fracture surface of broken specimens, surface analysis and volume analysis were carried out respectively by Optical Microscope (OM), Scanning Electron Microscope (SEM), 3D optical profilometer and 3D X-ray tomograph. Results of fatigue testing show a significant decrease of the HCF life mainly due to the surface roughness. Along with experimental testing, numerical simulations using FEM were conducted using the surface scans obtained by profilometry and tomography. Based on extreme values statistics of a non-local fatigue indicator parameter (FIP), a methodology is proposed to take into account the effect of the surface roughness on the HCF life.

Keywords: Roughness; Surface Modelling; Additive Manufacturing; Titanium alloys; Fatigue criteria

1. Introduction

In order to make the most of the additive manufacturing technologies, the fatigue behavior of additively manufactured materials has to be understood. Due to the quick development of this technology, a limited, yet fast evolving literature exists on this topic. Specimens obtained by SLM contain many defects that are

*Corresponding author nicolas.saintier@ensam.eu, Tel: +0033556845361

inherent to the process and impossible to eliminate even with the best process parameters monitoring [1–3]. Among these defects, porosity, surface roughness [4–6] and residual stresses [7, 8] are critical factors regarding the HCF strength.

Depending on their size and morphology, defects may lead to an early fatigue crack initiation. In the case of additive manufacturing it is well known that, before any post-treatment, the HCF strength of as-built specimens is not suitable for aircraft applications [9]. It is usually difficult to quantify and understand the respective influence of these defects since in many studies, the early crack initiation is due to a combination of parameters including porosity, surface roughness, residual stresses and specific microstructures [9–11]. Additively manufactured parts used for aircraft applications are almost systematically stress-relieved and post processed by HIP which reduces the effect of internal defects on the HCF behavior, but since the pressurizing medium impinges on the surface-connected porosity as though it was an extension of the surface, it does not change the possible impact on surface-connected defects [12]. On the other hand, surface roughness can not always be removed since the parts may have complex shapes. It is then very important to understand its effect on the HCF strength, and to propose a methodology for fatigue life prediction of rough surface effects under multiaxial loading.

Most of existing models [13–15] accounting for the effect of the surface roughness on the HCF strength consider the surface as a series of micronotches. The theoritical stress concentration factor induced by the notch $K_t = \left| \frac{\sigma_{loc}}{\sigma_{nom}} \right|$ is introduced, where σ_{loc} is the stress at the notch tip and σ_{nom} is the nominal stress. K_t can then be calculated using analytical formulations [16] or FEM. Since it is very difficult to measure the geometrical parameters needed to calculate the stress concentration factor for all the notches, Neuber et al [13] followed by Arola et al [14, 15] suggested analytical formulations to obtain the stress concentration factor based on surface roughness parameters. Theses models have proven efficient in predicting HCF strength. However, they require a periodic and homogeneous surface as obtained by machining and are therefore not applicable to additively manufactured surfaces. More recently, As et al [17] proposed a promising model where the HCF strength is predicted from 2D FEM using 3D topography measurements, the later methodology being applicable even to complex surface morphologies.

After stress relieving and HIP, the HCF behavior of as-built (i.e. rough) parts is governed by different competing factors. First, the surface roughness induces local geometrical discontinuities which act as stress concentrators. Secondly, high stress gradients occur resulting in a well known supporting effect regarding the HCF behavior [18, 19]. In the case of fatigue prediction of notched structures it is usually considered that the local stress at the notch tip is not suitable for fatigue life evaluation. In the general case, the effect of stress gradient at the notch tip can have several physical consequences, either on the local stress state (the presence of strong gradients modifies the development of local microplasticity as compared to smooth specimens), and, under certain conditions, on the development of non- propagating cracks. In both cases, in order to have cracks to initiate and overcome microstructural barriers, the stress state has

to be sufficiently high over a certain distance (or volume) from the highest loaded point. If not, cracks may initiate without propagating to a critical size from a structural point of view. Such observations were made by Frost et al [18] and Smith and Miller [19], who observed non-propagating cracks, measuring one to few grains at sharp notches, for an imposed stress lower than the endurance limit in the case of mild steel. Similar observations were made by Palin-luc et al [20] in the case of spheroidal graphite cast iron. Different methods can address this issue. Smith and Miller [19], El Haddad [21] and later Murakami [22–24] propose methods based on the Linear Elastic Fracture Mechanics framework. But these methods have shown mostly conservative results for uniaxial tension loading, require costly determination of ΔK_{th}, use the Linear Elastic Fracture Mechanics although it is a "short crack" problem and are not suitable for multiaxial loadings. In the case of the present study, since a multiaxial framework is aimed for the methodology, non-local fatigue life prediction methods have been preferred. They are basically based on two strategies: The averaging of the local stress on a given physical dimension, or, the explicit introduction of the local gradient in the fatigue criteria. Among others Taylor proposed three simple empirical approches to link the fatigue strength to the stress distribution: Point based method (PB); Line based method (LB); Volume based method (VB)[25, 26]. Nadot and Billaudeau [27] proposed a multiaxial fatigue limit criterion for materials with defects using the gradient of the hydrostatic stress. This criterion has been experimentaly validated for three different materials, three different type of defect and multiaxial loadings (torsion and combined tension-torsion). These methods using an isotropic homogeneous elastic or elastoplastic material behavior allow a good prediction of the fatigue limit of notched components even though the microstructure is of the same order of magnitude as the notch. The PB, LB and Nadot methods require specific directions along which stress gradients are considered to apply the methodology and are then difficult to apply when the morphology of the surface defect or the loading are complex. Since the VB method is easily applicable to any type of defect and allows for complex multiaxial loadings, it will be used in this study.

In order to take into account the role of microstructural heterogeneities in multiaxial fatigue life prediction, models have been developed in a probabilistic framework [28]. Recent models based on the extrem values (EV) distributions have given interesting results to establish a relationship between the microstructure characteristics and the variability of the fatigue behavior at the microstructural level [29, 30]. A similar approach is proposed here by describing the roughness induced stress heterogeneity at the specimen surface throughout an EV distribution that is used to predict the HCF behavior of as-built specimens.

This study aims to propose a general numerical methodology for fatigue life prediction of rough surfaces obtained by additive manufacturing. This methodology is based on the experimental evaluation of the HCF behavior of SLM stress-relieved HIP specimens with either machined or as-built surfaces. Along with experimental testing, numerical simulations using FEM were conducted using the surface scans obtained by profilometry and by tomography.

2. Materials and Methods

2.1. Studied Materials

Three sets of materials were studied: Hot-rolled (HR); SLM HIP machined (SLM machined); SLM HIP as-built (SLM as-built). All the SLM specimens were built on a EOS M280-2 in Z direction from Ti-6Al-4V titanium powder provided by ECKA GRANULES. The layers thickness is 30 μm and the process parameters are optimized to minimize defect density and residual stresses. All the specimens were stress-relieved (750°C 1 hour in Argon). The HIP treatment consists in applying an isostatic pressure of 120MPa (under argon) at a temperature of 920°C during two hours. This procedure allows eliminating both residual stresses and porosity. In addition, it homogenizes the microstructure of the samples in order to highlight the effect of the surface roughness.

The HR material, used as a reference, shows a fine equiaxed microstructure where the nodules are elongated along the rolling direction (RD) (Figure 1-a) and 1-b), a R_{p02} of $900MPa$ and a vickers microhardness (determined using norm iso 6507-1) equal to 316HV. The SLM HIP materials show a lamellar microstructure where the columnar ex-beta grains are still slightly distinguishable along the build direction and the α-lamellae thickness ranges from 1 to 3μm (see Figure 1-c). The R_{p02} is equal to $870MPa$ and the vickers microhardness to 316HV.

2.2. Experimental procedure

Fully reverse (R=-1) uniaxial tension/compression fatigue tests were conducted in load control using a sinusoidal waveform, in air at room temperature. These tests were conducted on a Zwick resonant testing machine, at 115Hz using the staircase method, in accordance with the ISO 1099 standard. The stop criterion was a frequency drop of 1Hz, which corresponds to a fatigue crack of approximately 3 mm in length, or a number of cycles equal to 2.10^6 2×10^6 cycles. An infrared camera SC4000 was used during the tests to ensure that there was no self-heating. The geometry of the SLM machined and SLM as-built specimens is given Figure 2- a. The geometry of the HR samples is given Figure 2-b. Pure torsion tests were performed on SLM HIP machined samples using an electromagnetic BOSE testing machine at 10Hz. Torsion fatigue tests were conducted under torque control with a load ratio R=-1, in accordance with the ISO 1352 standard. The stop criterion was an exceeding rotation angle of 1 degree which corresponds to a fatigue crack of a few mm or a number of cycles equal to 2×10^6 cycles. A compressed air cooling system was used to limitate self-heating of the samples. The geometry of the SLM machined samples for torsion tests is shown Figure 2-c. Machining specimens (figure 2-b and 2-c) were used to identify the fatigue crack initiation criterion on smooth specimens. Fatigue tests on as-built specimens (figure 2-a) are performed to evaluate the effect of surface roughness on HCF strength. In addition to that, tension fatigue tests (R=0.1) were conducted on SLM as-built (also HIPed) flat specimens on a Zwick resonant testing machine, at 80Hz. The geometry

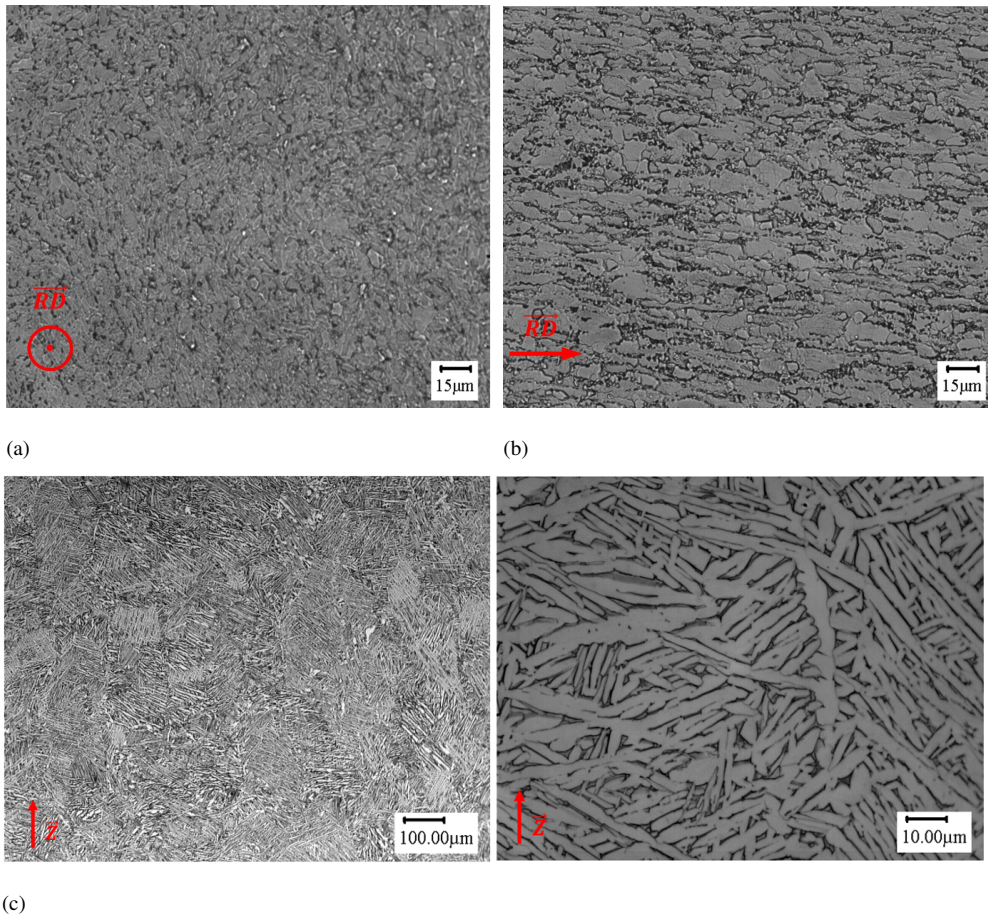

Fig. 1. Microstructure of: HR specimen perpendicular to the Rolling Direction (a); HR specimen parallel to the Rolling Direction (b) ; SLM HIP specimen at two different magnification (c). Z=Build direction.

of the specimens is given Figure 3. Two faces of the specimens were polished before each fatigue test to observe the crack initiations mechanisms at the surface.

2.3. *Strain-imposed cyclic tests*

To establish the cycle behavior of the SLM-HIP material, strain-imposed reverse tension cyclic tests were conducted at three different strain levels (0.8%; 1.0%; 1.3%) on a MTS servo-hydraulic testing machine at a f=0.1Hz frequency, on standard LCF machined specimens. Figure 4 shows the half-life cycle for respectively 0.8%, 1% and 1.3% of imposed strain. Using an optimization procedure, hardening laws were determined in order to correctly describe the experimental cycles. These laws will be used in the elastoplastic numerical simulations. The optimized hardening law are rather similar to the experimental data, except for the slight asymmetry between the tension and compression behavior which is not taken into account.

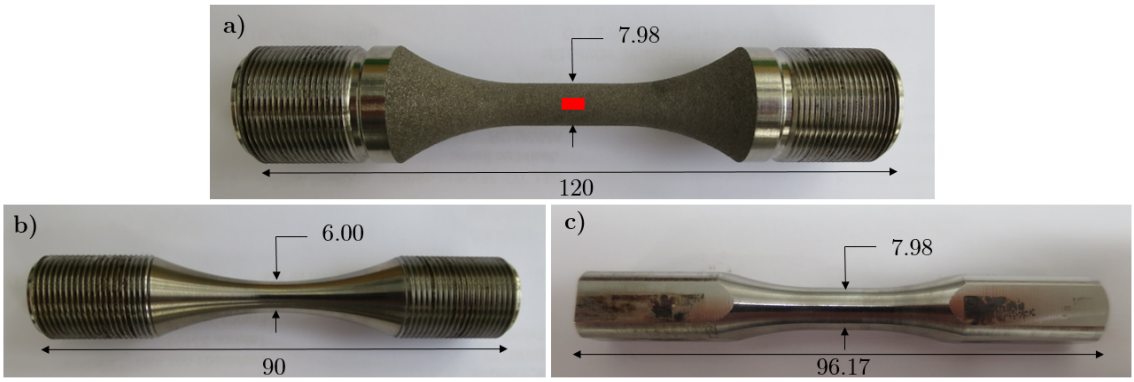

Fig. 2. Dimensions of the samples used for Fatigue tests. a) SLM machined and as-built used for fully reverse uniaxial tension/compression tests. The red rectangle shows the location of the surface scans; b) HR used for fully reverse uniaxial tension/compression tests; c) SLM machined specimens used for fully reverse torsion tests.

2.4. Surface analysis

In order to digitize the as-built surfaces, five SLM as-built fatigue specimens were partially scanned using a 3D Bruker Contour GT-K0-X optical profilometer. Four scans in the center of HCF specimens were carried out as shown Figure 2-a with a XY resolution of 2 μm and a Z resolution of 8 nm. Each scan measures 5 mm x 1.6 mm. The optical profilometer acquires approximately 80% of the points. The missing data are restored using a local least-squares method. Since the scanned surface is cylindrical, a flattening step is also applied. It consists of fitting the surface curvature with a quadratic surface of the form $ax^2 + bxy + cy^2 + dx + ey + f = z$ and removing this mean surface from the measured data. The result of the procedure is illustrated in figure 5. One should note that an optical profilometer is unable to fully capture the complexity of additivelly manufacture surfaces. Indeed, as illustrated on figure 6 that shows a micrography perpendicular to the surface, additive manufacturing induces a complex morphology that is not fully captured by optical profilometry. In order to assess the effect of this partial description of the surface, the surface morphology was also acquired by X-Ray tomography and both methodology where numerically evaluated. The voxel size is 2.5 μm and each scan measures 5 mm x 4.5 mm x 3 mm.

2.5. Numerical simulations

Numerical simulations aims at fully capture the complexity of the local stress-strain fields induced by the surface roughness and to introduce them into an HCF strength prediction methodology. The following sections describe the meshing and computations procedures and subsequent analysis.

2.5.1. Meshing

Meshed volumes and surfaces are created either from surface micrography, surface scans (profilometry) or volume scans (tomography).

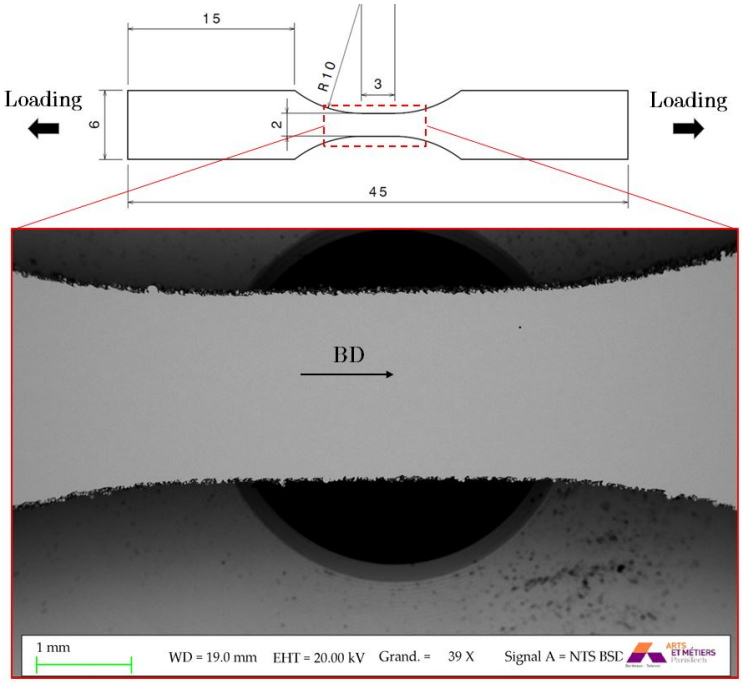

Fig. 3. Dimensions of the SLM as-built flat samples used to observe the crack initiation mechanisms occuring during fatigue tests (R=0.1).

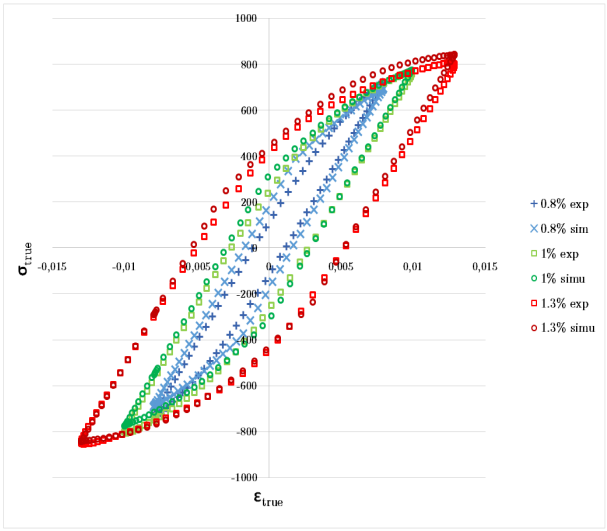

Fig. 4. Experimental and numerical stabilized stress-strain curves of SLM machined specimens at 0.8% 1% and 1.3% of imposed strain.

- Meshed surfaces from micrographic analysis: Micrographic observations allow a very accurate surface roughness description. To simulate a real-surface profile, a meshed surface was created using micrographic analysis. The surface was precisely-fitted by using b-spline so that the meshed surface

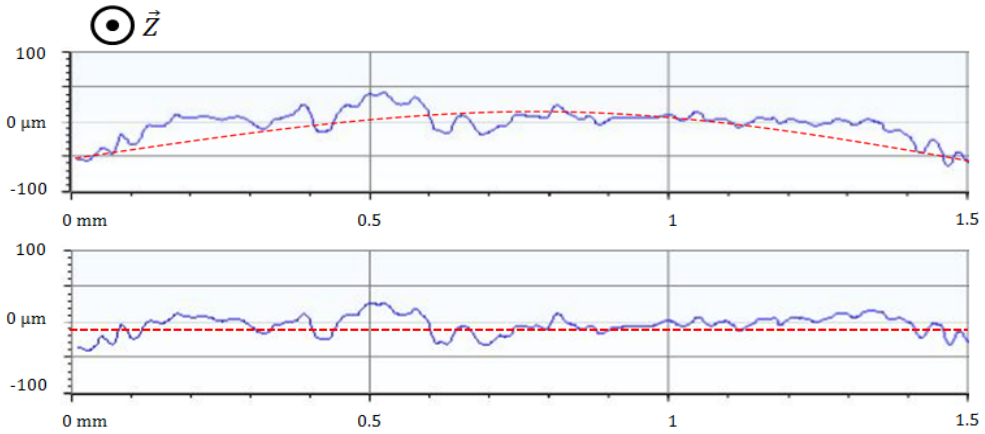

Fig. 5. Profilometric data on a cylindrical specimen before and after flattening procedure.

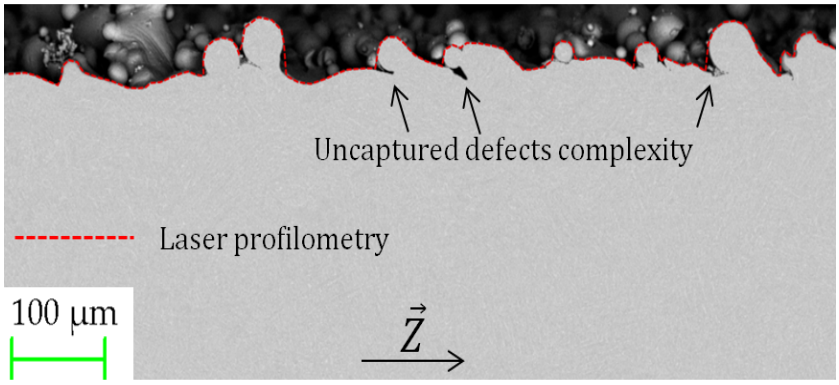

Fig. 6. Micrography of a SLM as-built surface and associated profilometric measurement.

shows a very fine mesh where the curvature is important. 4 mm long profiles containing 100 000 elements with quadratic interpolation were created as shown figure 7.

- Meshed volumes from profilometric scans: In order to build meshed volumes suitable for calculation and having a surface morphology matching the as-built surface, the surface data were filtered. A Gaussian Regression Filter (high pass, cutoff: 20 μm) and a Statistical Median Filter (range 8 pixels) were applied. Figure 8-a) shows the effects of the filters from raw data to a usable profile. The comparison of a typical filtered profile Figure 8-a) and a typical profile obtained from micrography 8-b) shows that the global aspect of the two profiles are very similar. Since the two extracted profiles were not generated from the exact same location of the sample they are not supposed to be identical. Each scans is divided into ten surfaces of 0.3x0.4mm and from each surface a meshed volume is generated (0.3x0.4x0.5 mm). Each volume contains approximately 1 300 000 tetrahedral elements with quadratic interpolation, which ensure the convergence of the mesh. The size of the elements

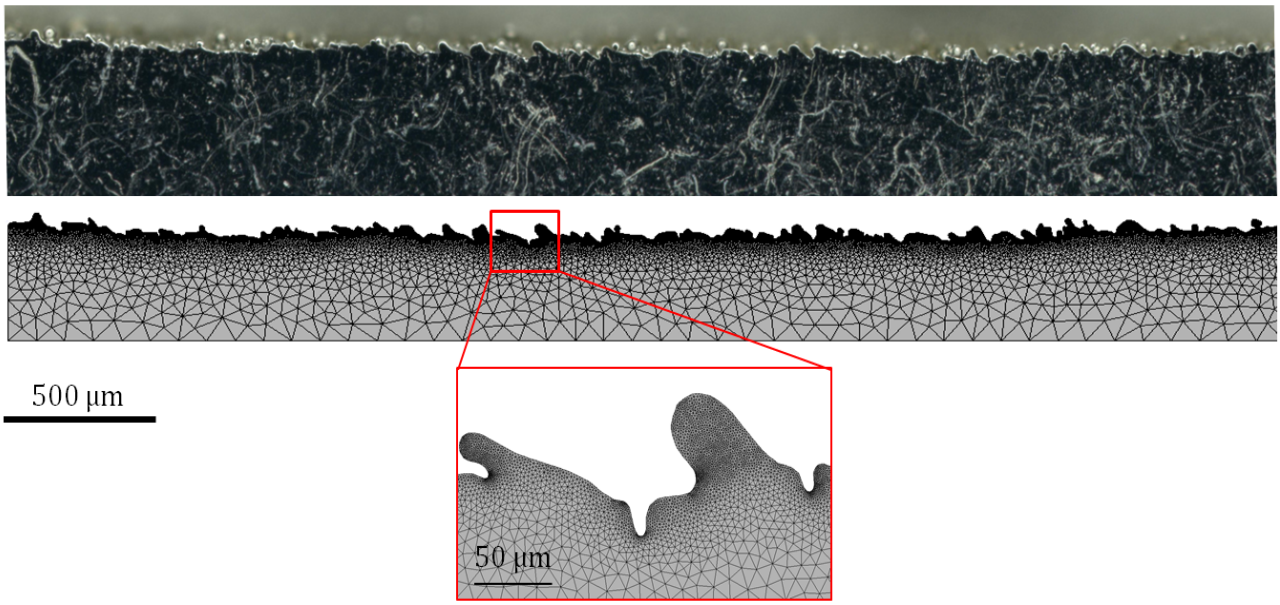

Fig. 7. Micrography of a SLM specimen surface and associated 2D profile

located on the surface is 2 μm (side) which corresponds to the XY resolution of the scans (Figure 9-a).

- Meshed volumes from tomographic scans: The surface of the scaned volume is first extracted and smoothed using Aviso software, a meshed is then generated using Gmsh [31]. The size of the elements located on the surface is 2.5 μm which corresponds to the voxel size of the scans. For a cube of 180 μm of side, more than 100 000 elements with quadratic interpolation were created (Figure 9-b).

2.5.2. *Calculations settings*

FE computations were conducted using the FE code Zebulon. Due to the complexity of the surface topology, high local stresses are expected to occur at the surface. In order to evaluate the effect of local plasticity on the near surface stress fields, two different constitutive models were considered: isotropic elasticity and elastoplastic behavior. In the case of elasticity, a Young's modulus of 110 GPa and Poisson's ratio of 0.34 were considered. In the case of cyclic plasticity, an Armstrong Frederic [32] model including two non linear kinematic hardenings and one isotropic hardening was chosen in order to fit experimental data. The yield function is given by:

$$f_{\text{vm}}(\bar{\bar{\sigma}}, \bar{\bar{X}}, R) = \sqrt{\frac{3}{2}(\bar{\bar{\sigma}}^d - \bar{\bar{X}}^d) : (\bar{\bar{\sigma}}^d - \bar{\bar{X}}^d)} - R \tag{1}$$

where $\bar{\bar{\sigma}}^d$ is the deviatoric part of the stress tensor, $\bar{\bar{X}}^d$ the deviatoric part of the kinematic hardening stress tensor calculated using equation 2 and 3, and R the isotropic hardening calculated using equation 4.

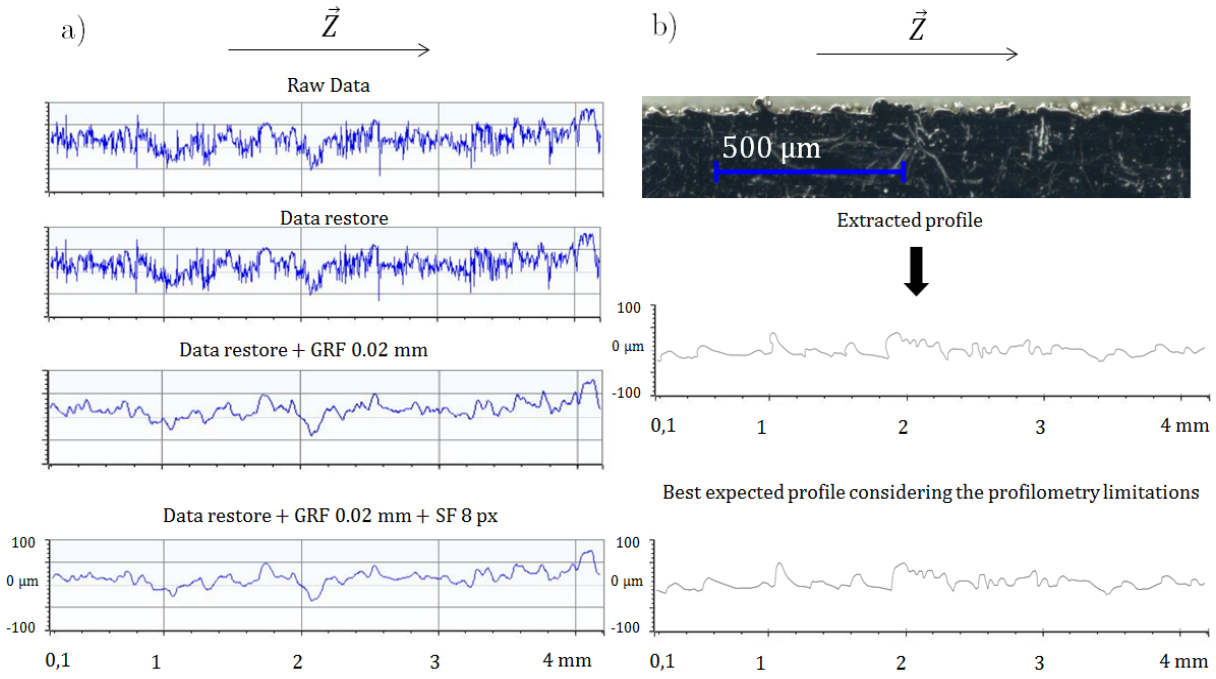

Fig. 8. Comparison of a typical surface profile obtained by profilometry a) to a typical expected surface profile obtained from micrography b).

Table 1. Parameters of the elastoplastic model

Parameter	E	ν	C_1	D_1	C_2	D_2	R_0	K
Value	110 GPa	0.34	$1.0e^5$ MPa	$3.0e^2$	$1.4e^{-2}$ MPa	$1.45e^2$	$5.41e^2$ MPa	$-1.06e^2$ MPa

$$\bar{\bar{n}} = \frac{3}{2}\frac{\bar{\bar{\sigma}}^d - \bar{\bar{X}}^d}{f_{\text{vm}}} \tag{2}$$

$$\bar{\bar{m}}_{kin} = \bar{\bar{n}} - \frac{3D}{2C}\bar{\bar{X}} \tag{3}$$

$$R = R_0 + K(e_0 + p) \tag{4}$$

Table 1 summarizes the parameters identified from the experimental cyclic behavior obtained from strain-imposed cyclic tests. Using Numerical computations were performed on each meshed volumes to reproduce the experimental fatigue loading (R=-1) ensuring that the nominal maximum axial stress in the computed volume was equal to the nominal cylic maximum axial stress of HCF tests. In the case of elasto-plastic behavior, 2 cycles where sufficient to fully stabilize the local stress strain state. Figure 10 shows

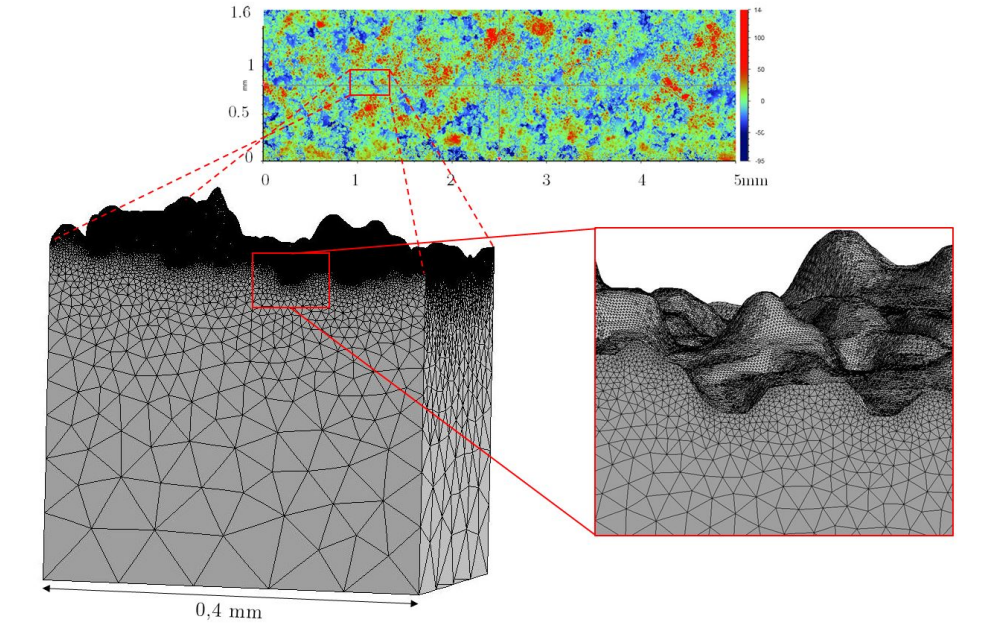

(a)

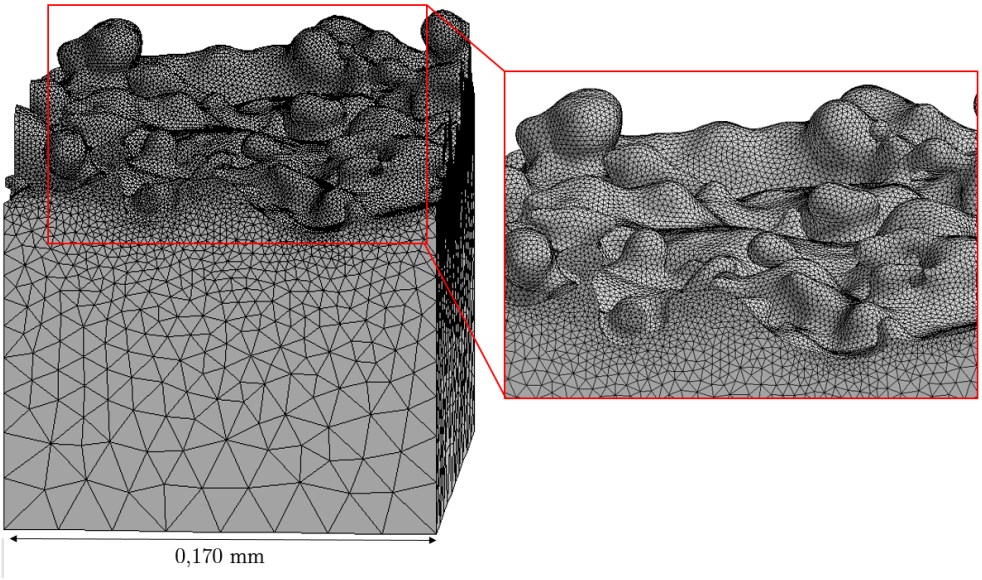

(b)

Fig. 9. Meshed volume generated from a surface scan (profilometry) (a). Meshed volume from volume scan (tomography)(b).

the simulated σ_{11} stress field within a volume for an experimental applied nominal maximum stress of
200 σ_{max} = 222.5 MPa which corresponds to the fatigue limit of SLM as-built specimens.

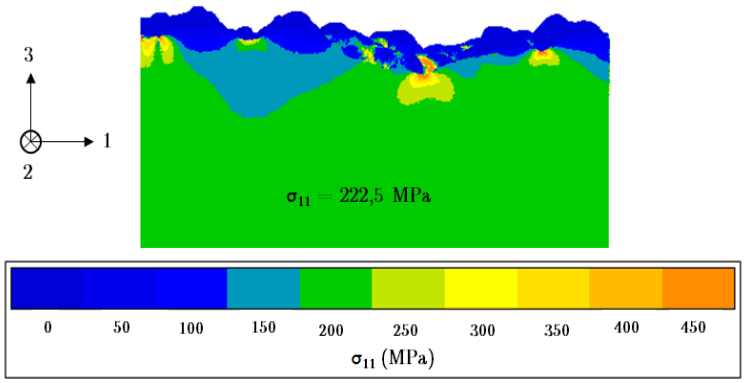

Fig. 10. Simulated σ_{11} stress field within an volume for an experimental applied nominal maximum stress of 222.5 MPa.

2.5.3. *Mesoscopic Fatigue Indicator Parameter (FIP)*

Since the fatigue loadings considered in this work are relatively simple (tension, torsion loading), even considering the multiaxial stress state induced by the presence of micronotches, the choice of the fatigue criterion is not crucial. Among the possible choices, the Crossland criterion was chosen for its simplicity and low computational cost. The local stress-based Crossland criterion [33] is a linear combination of the amplitude of the second invariant of the deviatoric tensor $\tau_{oct,a}$ and the maximum value of the hydrostatic stress over a cycle $\sigma_{H,max}$ (equations 5, 6 and 7). Based on the Crossland criterion a fatigue indicator parameter is proposed as follows:

$$FIP_{cr}(M) = \tau_{oct,a}(M) + \alpha\sigma_{H,max}(M) \tag{5}$$

with:

$$\tau_{oct,a}(M) = \sqrt{\frac{1}{2}\max_{t\in T}\left[\bar{\bar{S}}(M,t) - \bar{\bar{S}}_m(M)\right] : \left[\bar{\bar{S}}(M,t) - \bar{\bar{S}}_m(M)\right]} \tag{6}$$

$$\sigma_{H,max}(M) = \max_{t\in T}\left[\frac{1}{3}Trace(\bar{\bar{\sigma}}(M,t))\right] \tag{7}$$

where $\bar{\bar{S}}(M,t)$ is the deviatoric stress tensor and $\bar{\bar{S}}_m(M)$ the mean deviatoric stress tensor. As said previously, the presence of micronotches induces high local stresses and gradients that must be considered to assess the fatigue strength of as-built (rough) parts. In the proposed approach, the gradient effect is taken into account by using a non local FIP consisting in the volumetric averaging of the local FIP at each gauss point of the FE model. The non local FIP, based on the Crossland criterion can then be expressed as follows:

$$\langle FIP_{cr}(M)\rangle = \langle\tau_{oct,a}(M)\rangle + \alpha\langle\sigma_{H,max}(M)\rangle \tag{8}$$

with:

$$\langle\tau_{oct,a}(M)\rangle = \frac{1}{V_c}\iiint_{V_c}\tau_{oct,a}(M)dV \tag{9}$$

$$\langle \sigma_{H,max}(M) \rangle = \frac{1}{V_c} \iiint_{V_c} \sigma_{H,max}(M) dV \tag{10}$$

where V_c is the averaging volume. In our case, V_c was considered as a sphere of radius D_c centred on M, so that:

$$\langle \tau_{oct,a}(M) \rangle = \frac{1}{\frac{4}{3}\pi D_c^3} \int_{\theta=-\pi}^{\theta=+\pi} \int_{\phi=0}^{\phi=2\pi} \int_{r=0}^{r=D_c} \tau_{oct,a}(M) sin\theta r^2 dr d\theta d\phi \tag{11}$$

$$\langle \sigma_{H,max}(M) \rangle = \frac{1}{\frac{4}{3}\pi D_c^3} \int_{\theta=-\pi}^{\theta=+\pi} \int_{\phi=0}^{\phi=2\pi} \int_{r=0}^{r=D_c} \sigma_{H,max}(M) sin\theta r^2 dr d\theta d\phi \tag{12}$$

This approach was already used by the authors for gradient effect induced by piting in the case of fatigue corrosion [34] and in the case of surface defects induced by a punching process [35]. The fatigue strength is considered to be reached when, at a point M of the considered volume, the following condition is fulfilled:

$$\langle FIP_{cr} \rangle_M = \beta \tag{13}$$

or when:

$$C_d(M) = \frac{\langle FIP_{cr} \rangle_M}{\beta} = 1 \tag{14}$$

where β is a material parameter associated to a given failure probability at a given number of cycles and C_d the danger coefficient. α and β are material parameters evaluated from two fatigue strengths (tension R=-1 and torsion R=-1 in our case) and at a failure probability of 0.5. The identification of the D_c critical distance is presented in section 2.5.4.

2.5.4. Generalized Extreme Values Distribution

As shown on figure 10, surface roughness induces a strong heterogeneity of the local stress field. The fatigue strength is driven by the most loaded points at the surface of the material, ie the material points exhibiting the highest FIP or C_d parameter. As with previously proposed methodologies for the statistical evaluation of FIP field obtained from fullfied microstructure modeling [30], a generalized extreme values (GEV) statistic framework is proposed to describe the extreme FIP population of rough surfaces.

For every volume (or surface for 2D calculations), local maximums of the FIP are numerically extracted. As one would expect, they are located at the surface. Extracted material points can not be closer than 50 μm, in order to have approximately one EV per notch. The EV distribution being slightly different when

extracted from two different volumes, it is not possible to consider each volume as a Representative Volume Element (RVE) from the fatigue point of view. Instead, each volume has to be considered as a Statistical Volume Element (SVE) from which part of the global extreme value data will be obtained. The global EV data set was obtained from the concatenation of EV on each SVE:

- Between 30 and 40 EV were extracted on each 2D profile and computations were performed on 4 different 2D profiles (143 EV in total).
- Between 15 and 25 EV were extracted on each SVE from profilometry and computations were performed on 20 different SVE (451 EV in total).
- Between 8 and 10 EV were extracted on each SVE from tomography and computations were performed on 3 different SVE (32 EV in total).

For each condition (2D, profilometry, tomography), the extreme values are gathered and the obtained distribution is fitted using the GEV methods (see [30] for more details on these methods). The median of the fitted distribution will be used in this study to evaluate the HCF strength and will be noted: $\langle FIP_{cr} \rangle_{p=0.5}$ The critical distance D_c is chosen so that $\langle FIP_{cr} \rangle_{p=0.5}$ for 2d calculations is equal to β. This procedure leads to a $D_c = 2\mu$m value. The impact of the critical distance over the distribution of non-local values is illustrated Figure 11. The higher D_c, the lower the non-local values since gauss-point located further from the notch tip will be used in the averaging procedure. The 2d micrographic surface is used as reference since this surface description combines a significant number of micro notches (and subsequent hot-spots) and a proper description of the surface morphology even if the 3D nature of the surface is not captured.

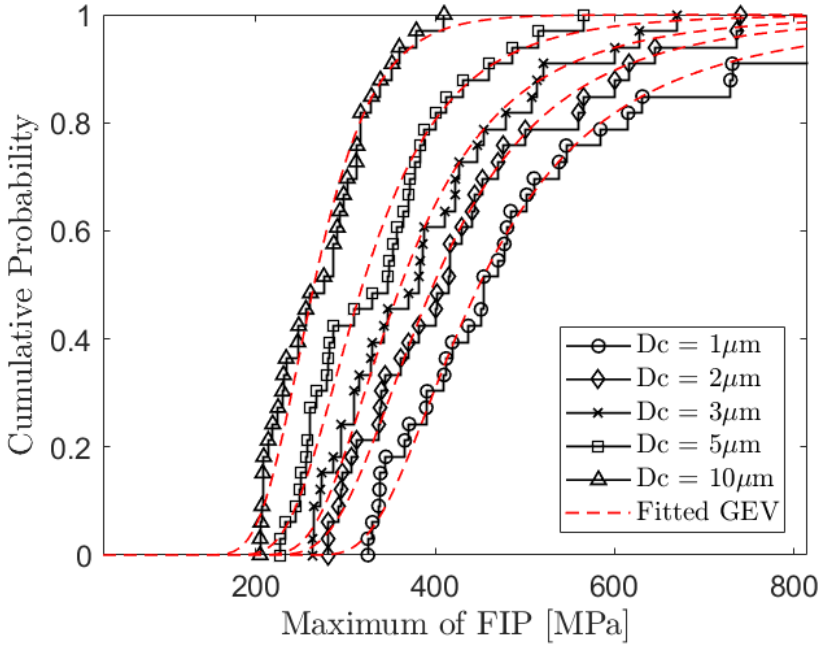

Fig. 11. Distribution of the E.V. of the FIP and associated fitted G.E.V.distribution for different critical distances

3. Results and Discussions

3.1. HCF Tests

Figure 12 illustrates the fatigue results obtained for uniaxial tension/compression loading conditions. The HR specimens show the highest fatigue strength, as expected according to the fine equiaxed microstructure, which is very suitable for fatigue applications [36]. The reduced fatigue strength of machined SLM specimens compared to HR specimens is due to the change in microstructure (from fine equiaxed to fully lamellar). The drop in term of maximum stress is about 100 MPa over the total investigated fatigue life range, which corresponds to more than a decade in term of fatigue life. The effect of surface roughness is tremendous since it induces a drop of more than 60% of the fatigue strength. The difference between the SLM machined and SLM as-built fatigue limit is due to the surface notches which act as stress concentrators. One should also note that the machining process most likely generates compression residual stresses [37] but this has not be taken into account in this study.

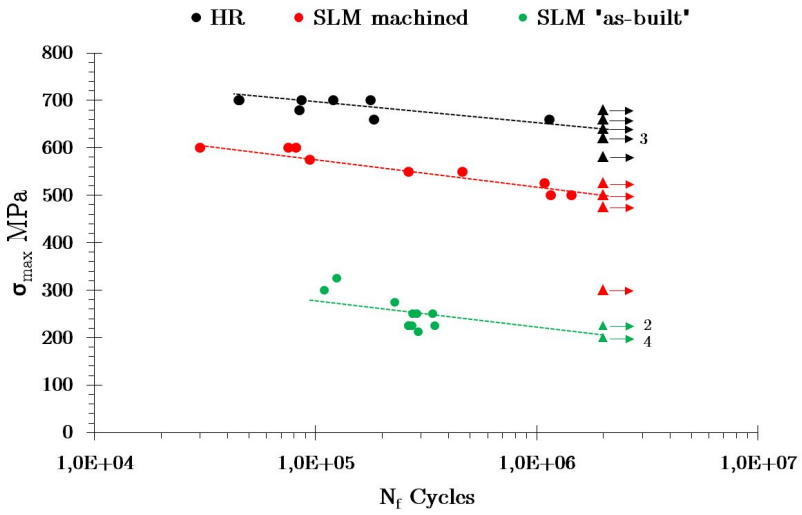

Fig. 12. S-N curves of the three sets of specimens. Fully reversed uniaxial tension/compression tests R=-1; f=115Hz; Max number of cycles = 2×10^6.

specimens	**HR**	**SLM machined**	**SLM as-built**
σ_d (MPa)	675.5	512.5	222.5
SD (MPa)	18.1	28.2	10.9

Table 2. Fatigue strength and associated standard deviation of the tested sets of specimens at 2×10^6 cycles, R=-1 and f=115Hz

In addition, fully reversed torsion tests were performed on SLM machined samples in order to determine the fatigue limit which will be used in the numerical simulations. The fatigue limit at 2×10^6 cycles

determined by the stair case method from 9 specimens is 417 MPa with an associated standard deviation of 41 MPa.

3.2. Fractography analysis

Authors report that, when the HIP post-processing has not been applied, fatigue cracks in additively manufactured titanium alloys generally initiate from porosities located close to the surface for machined specimens and from surface defects for as-built specimens, respectively [38]. HIPed and machined specimens initiate from microstructural heterogeneities located at the specimens surface or occasionally from sub-surface internal porosities not removed during HIP [39]. In this study, SEM observations show that fatigue crack initiation sites are always located at the specimens surface. In the case of machined specimens, fatigue crack initiation always occurs from microstructural heterogeneities located at the specimen surface (Figures 13-a and 13-b), confirming the drastic shrinkage of porosities after HIP process. In the case of as-built specimens, out of 9 broken samples, 7 show a fatigue crack initiation induced by the surface roughness (Figure 13-d) and 2 a fatigue crack initiation induced by a lack of fusion defect ($\sqrt{area} \approx 160\mu m$) remaining at the surface (Figure 13-c). Observations conducted on flat samples tested in fatigue at R=0.1 show that, after the HCF test at the endurance limit, in addition to a main crack that led to the failure of the specimen, there are also numerous non-propagating cracks measuring between 5 and 10μm initiated from local notch tip. This indicates that the surface is composed of many sharp notches and that a local stress value is sufficient to initiate but not to propagate, and so not appropriate for direct estimation of the fatigue limit of as-built specimens.

3.3. Characterization of the near surface stress field

3.3.1. Distribution of local values

Whatever the modeling method, surface roughness induces a high number of micronotches. Each micronotch locally modifies the stress field so that stress levels near the notch tip are much higher than the applied nominal maximum stress. Figure 15 shows the distribution of the octahedral shear stress calculated at each Gauss point within a volume obtained from profilometry for an applied nominal maximum stress σ_{11} of 222.5 MPa for both elastic and elastoplastic computations. Gauss points having a value of τ_{oct} = 128 MPa are located within the volume sufficiently far from the rough surface to be nonsensitive to the notch effect. Gauss points having a value of τ_{oct} close to 0 are located within a bump of the rough surface. It shows that some of the material is inefficient from a mechanical point of view. The high values of τ_{oct} are attributed to Gauss points located at the surface, close to micronotches acting as stress concentrators. The difference between elastic and elastoplastic calculations is highlighted for values of τ_{toct} being greater than $R_0/\sqrt{3}$, which concern less than 0.5% of the Gauss points. Since plasticity affects the most loaded points, it may significantly modify the EV distribution despite a small impact on the global stress distribution. Figure

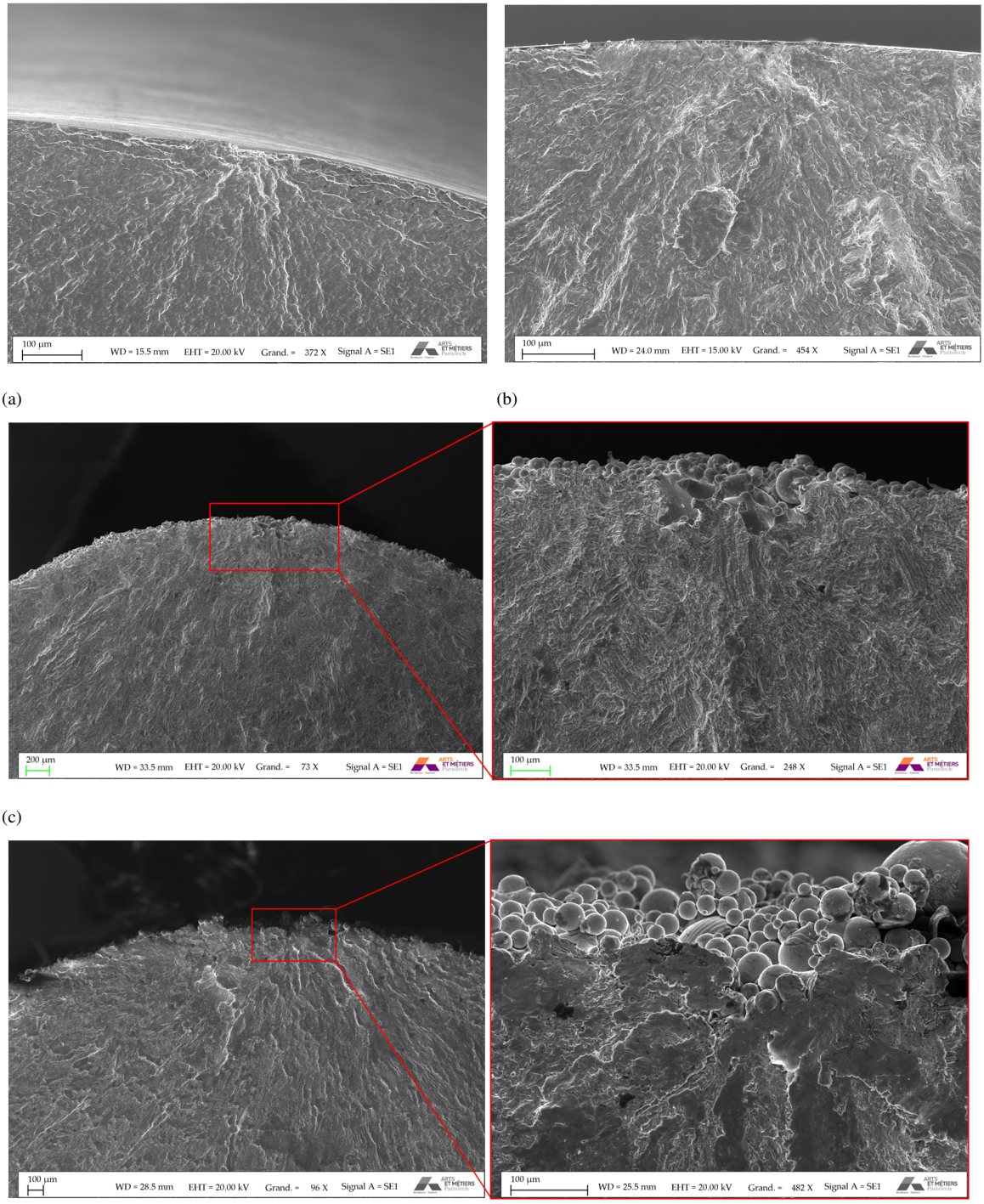

Fig. 13. Fracture surface of: an HR machined specimen, 84749 cycles, 680 MPa (a); a SLM machined specimen, 262751 cycles, 550 MPa (b) ; a SLM as-built specimen, 291965 cycles, 212.5 MPa (c) ; an SLM as-built specimen, 109201 cycles, 300 MPa (d).

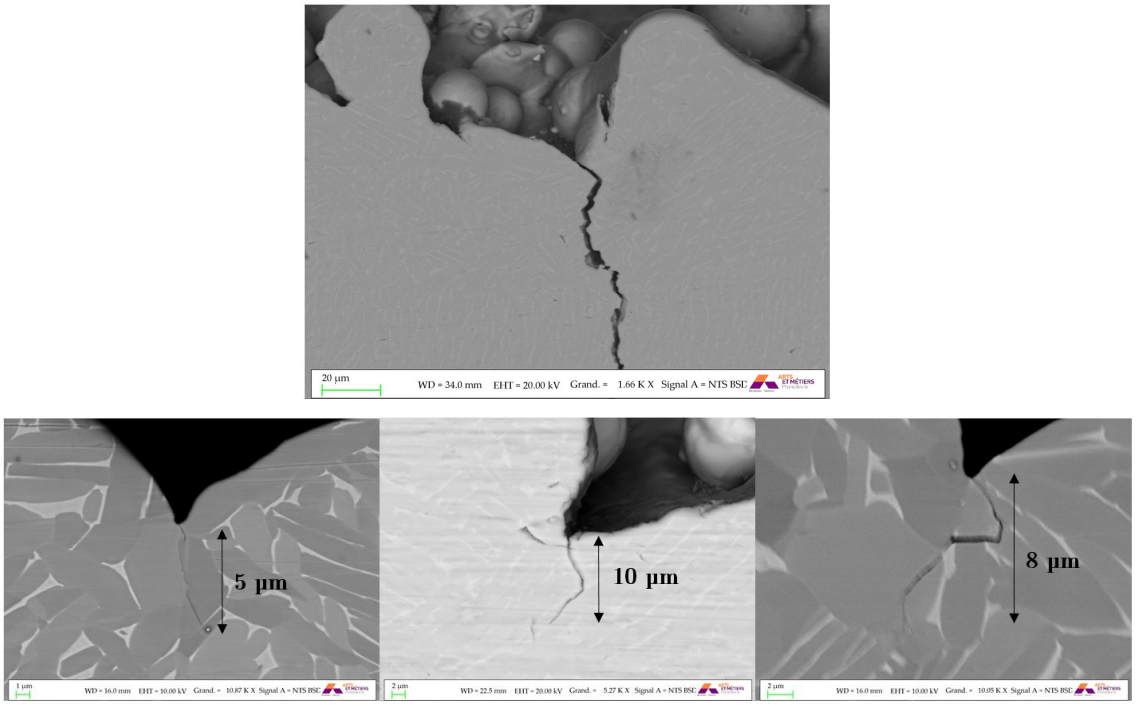

Fig. 14. Observations of surface crack initiation on flat SLM as-built specimens tested in tension (R=0.1): Main crack and non-propagating cracks.

16 illustrates the impact of the constitutive law on the EV distribution of τ_{oct} obtained either from the same SVE or from the gathered distribution of all SVE. In this SVE, only 9 micronotches induce cyclic plasticity. It means that plasticity is localized in some specific regions at the surface and does not concern all EV locations.

3.3.2. *Effect of the volume averaging*

Volume averaging over a critical distance is a way to take into account the gradient effect. The larger the stress gradient, the higher the effect of the averaging procedure on the local stress state. Figure 17 shows the probability density function of the EV of τ_{oct} extracted from the same SVE for elastic computations. When averaging, the whole distribution is shifted to lower values and the difference between local and non local values is higher for the high value of the EV. This shows that in this case, higher EV are also associated to higher local stress gradient. Since the plasticity is very local, the averaging procedure drastically reduces the difference between the distribution of EV for elastic and elastoplastic calculations. As shown Figure 17, the distributions of non local octahedral shear stress are very similar for both calculations, in the HCF regime, so that the choice of the constitutive model will not significantly impact the FIP considered in the HCF criterion.

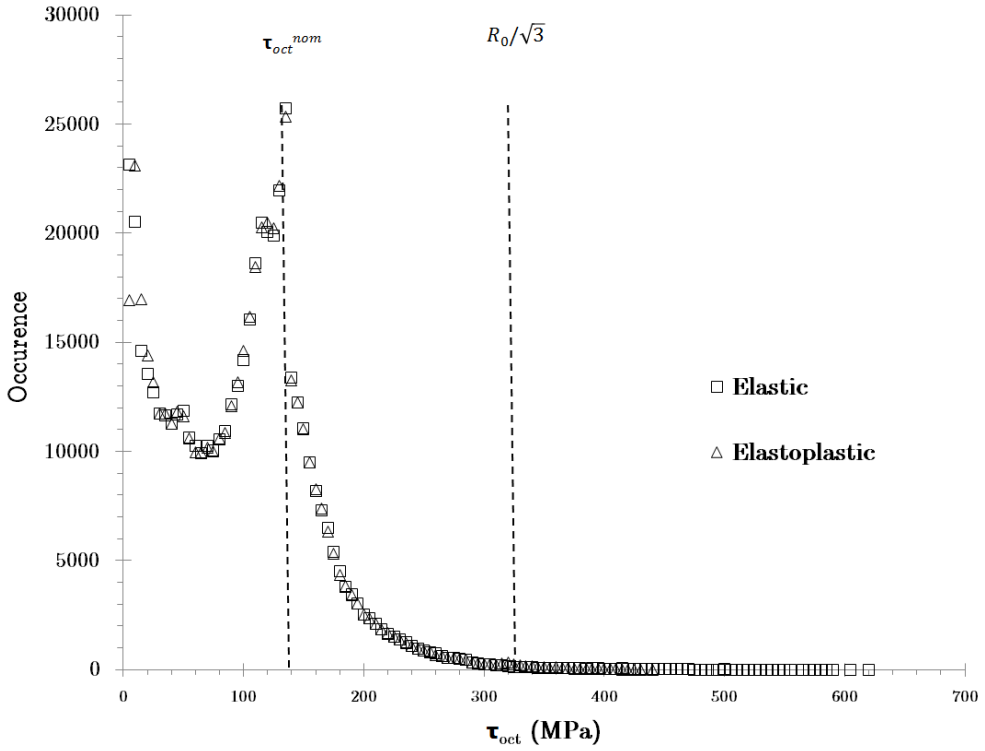

Fig. 15. Distribution of τ_{oct} within an SVE obtained from profilometry for an applied nominal maximum stress σ_{11} = 222.5 MPa

3.3.3. Gradients at the notch tip

Stress gradients at the notch tip depend on the micronotch geometry which is determined by the surface acquisition procedure (micrography, profilometry or tomography). Figure 18-a shows the Von Mises equivalent stress gradient associated to two different micronotches obtained using micrographic analysis and elastoplastic calculations. Since there are many notch geometries, it is possible to define a Grey zone within which all stress distributions will be contained. The distance affected by the gradient ranges from 10 to 50 μm.

The variability of the gradient associated to 2d calculations is also noticeable in volumes obtained from profilometric and tomographic scans but the highest stress gradients are observed in 2d (Figure 18-b). This is certainly due to the filtering steps used to build volumes using profilometric scans, suitable for calculations. Figure 18-b shows the Von Mises equivalent stress gradient associated to the highest Von Mises value within an SVE obtained by each method. The gradient in SVE obtained from all the methods are rather similar but it can be seen that lower gradient are associated to calculations from profilometric scans. The typical notch root radius associated to SVE obtained from profilometric analysis is bigger which is also a consequence of the filtering steps. Figures 19-a and 19-b show the danger coefficient distribution in the vicinity of a typical micronotch within an SVE obtained respectively from profilometric and tomographic analysis.

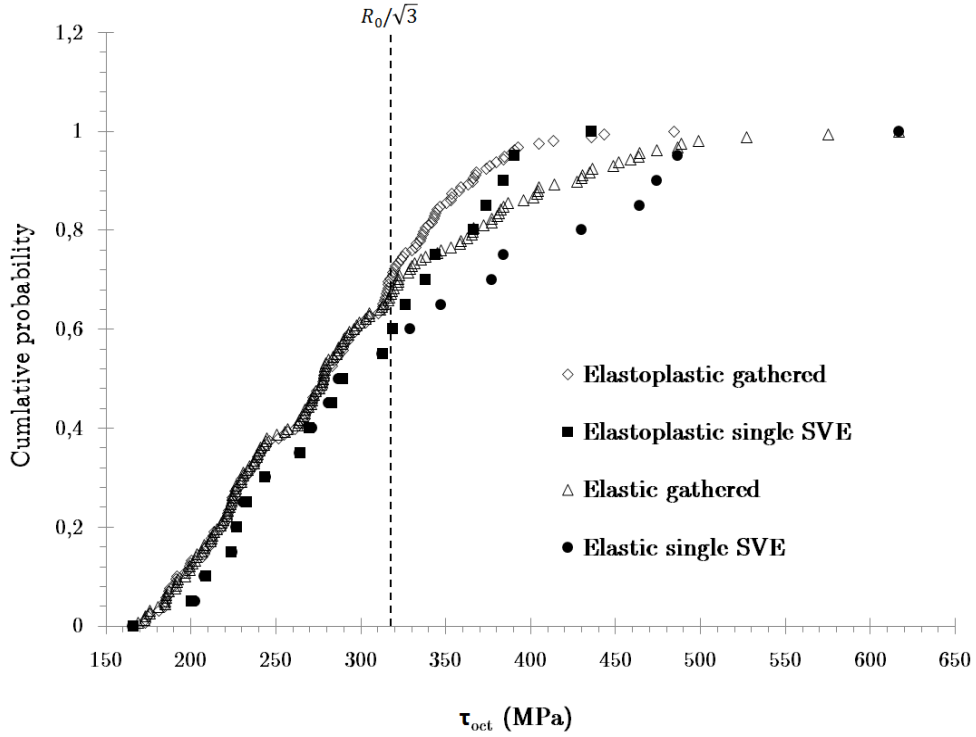

Fig. 16. Cumulative probability function associated to the EV of τ_{oct} within an SVE obtained from profilometry for an applied nominal maximum stress σ_{11} = 222.5 MPa

The gradient of cumulated plastic deformation per cycle associated the highest plastic deformation value within a SVE is illustrated Figure 20. It shows that the plastic gradient in SVE's obtained from profilometric and tomographic analysis is very similar whereas the plastic gradient associated with 2d computations is way bigger. Indeed, due to the hardening law associated with our material, $\frac{d\epsilon_p}{d\sigma_{vm}}$ becomes higher when $\sigma_{vm} > 750$ MPa so that the small difference regarding σ_{vm} between 2d and 3d calculations leads to a huge difference regarding $\Delta\epsilon_p$. In the later condition, the maximum size of the plastic zone is approximately equal to 2 μm which corresponds to the critical distance D_c. The calculations using tomographic and profilometric analysis give much lower plasticity levels but the plastic zone associated with the most critical notch within an SVE is the same for all methods.

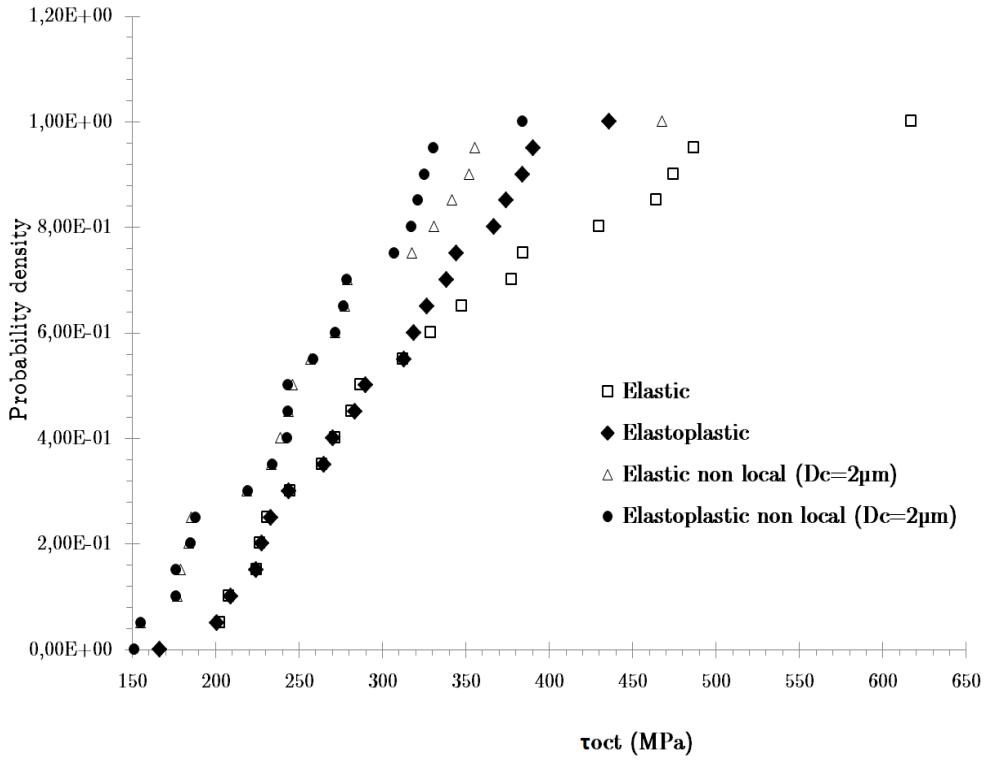

Fig. 17. Distribution of $\langle \tau_{oct} \rangle$ EV within an SVE obtained from profilometry for an applied nominal maximum stress $\sigma_{11} = 222.5$ MPa

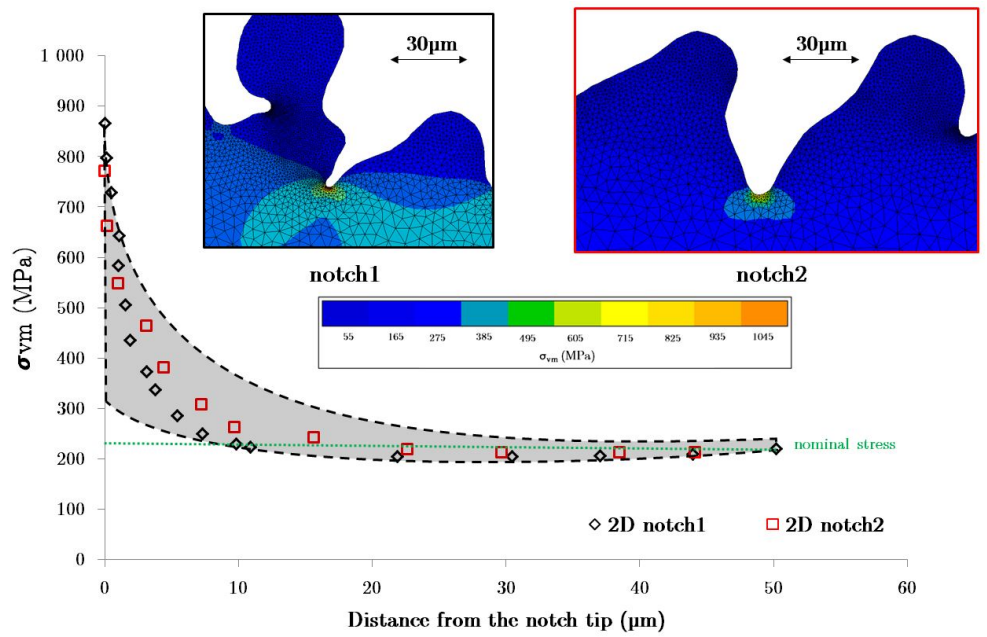

(a)

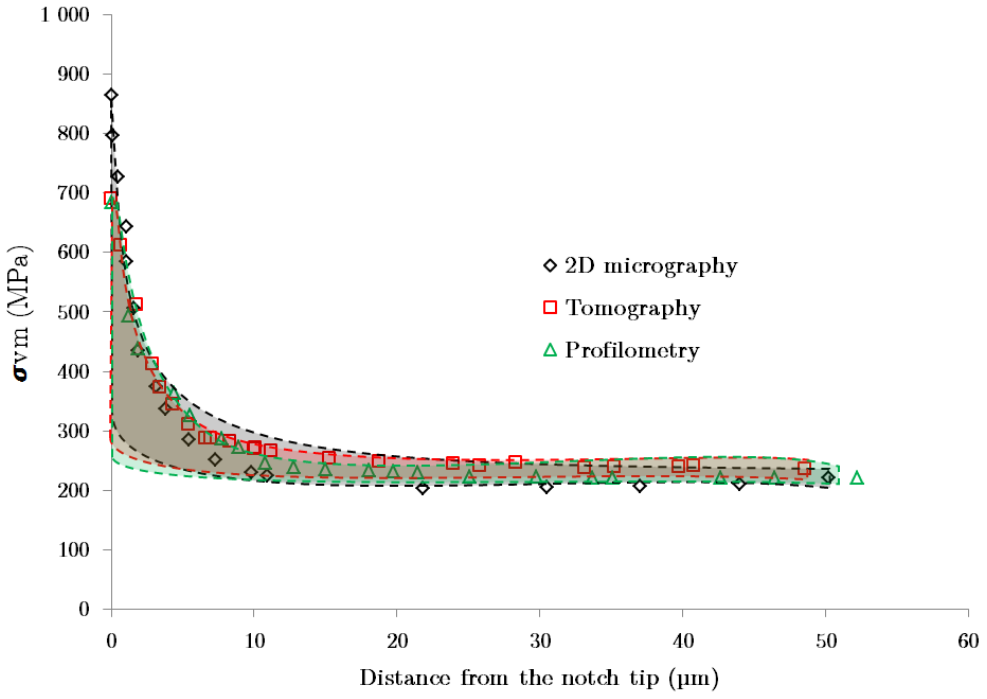

(b)

Fig. 18. Von Mises equivalent stress as a function of the distance from the notch tip for two different notches within an SVE obtained from micrographic analysis and for an applied nominal maximum stress σ_{11} = 222.5 MPa (a). Von Mises equivalent stress as a function of the distance from the notch tip for 3 SVE, each one associated with a different surface analysis method (b).

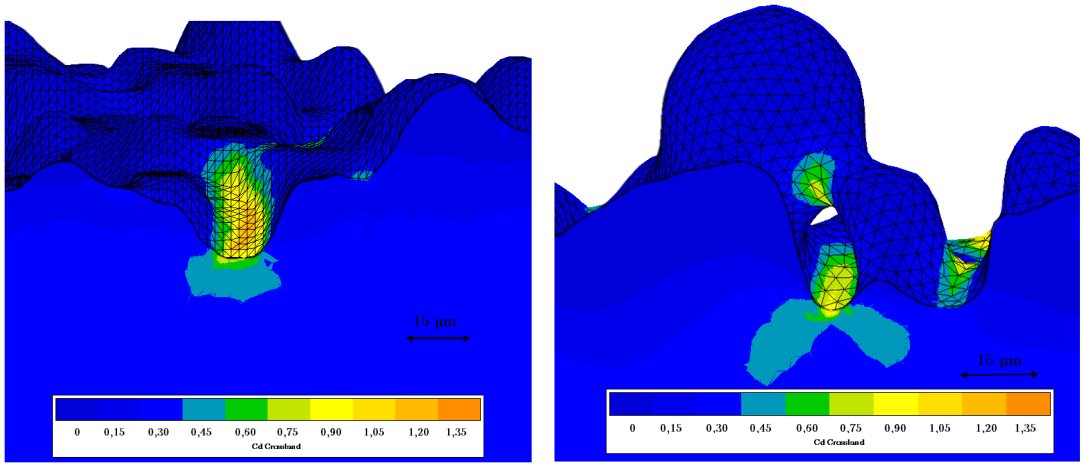

(a) (b)

Fig. 19. C_d distribution in the vicinity of a notch within a SVE obtained from profilometric analysis (a) and tomographic analysis (b).

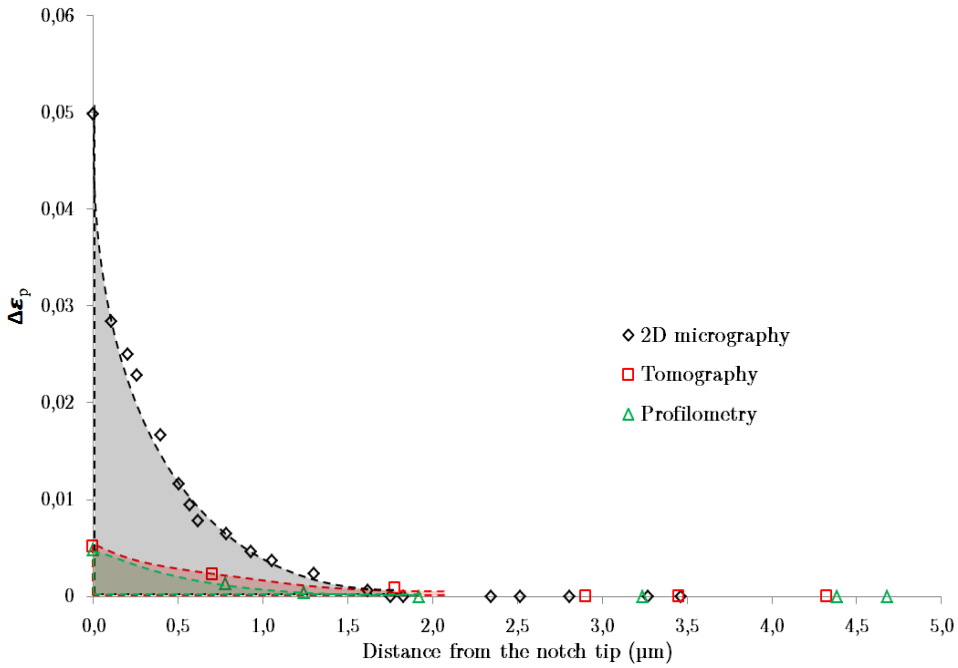

Fig. 20. ϵ_{pcum} as a function of the distance from the notch tip for 3 SVE, each one associated with a different surface analysis method.

3.4. GEV and HCF behavior

Figure 21 shows the Crossland diagram associated to a SVE obtained from micrographic analysis and for an applied mean stress σ_{11} = 222.5 MPa. Before the averaging procedure, most of the EV are located above the threshold. Based on these values, the loading appears to be very critical regarding fatigue (failure probability > 0.5) even though the applied loading corresponds to the fatigue strength. The averaging procedure brings the highest values closer to the threshold, leading to a more accurate prediction of the criticity of the stress state regarding HCF. The EV (with black borders on figure 21) are extracted and fitted using the GEV methods. The probability density function associated to the distribution of EV is shown Figure 22. As presented in section 2.5.4, the averaging procedure allows to obtain for non local EV a median close to β. Since the plastic zone in the most critical case is approximately the same size as D_c, the median of non local GEV distribution for elastic and elastoplastic calculations is almost the same as it can be seen Figure 22. This is valid for an applied mean stress σ_{11} = 222.5 MPa. When the applied mean stress is higher, the difference between elastic and elastoplastic calculations is more and more highlighted.

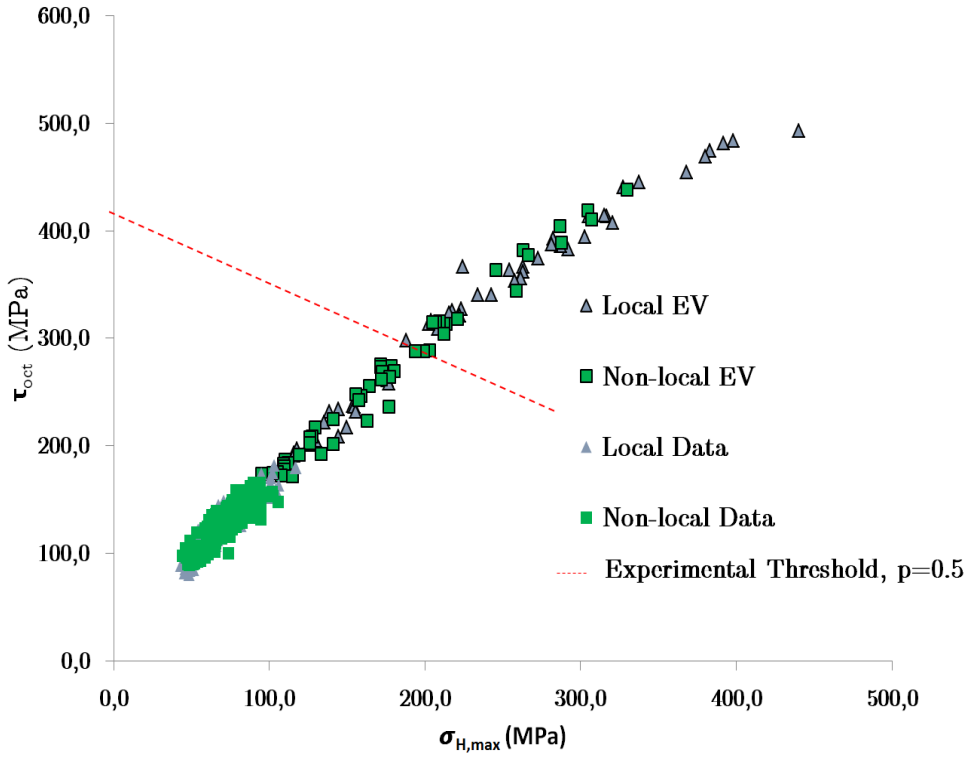

Fig. 21. Crossland diagram associated to a SVE obtained from micrographic analysis and for an applied nominal maximum stress σ_{11} = 222.5 MPa.

Figure 23-a shows the synthesis of the calculations conducted within SVE obtained from profilometric analysis. The distribution of the $\langle FIP_{cr} \rangle$ at the surface of the SVE obtained from profilometric analysis

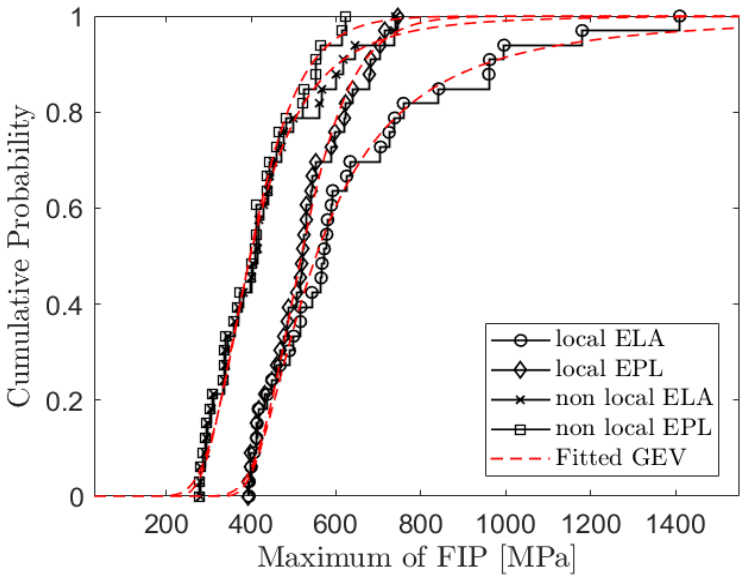

Fig. 22. Cumulative probability function of the local and non local FIP distribution for 2d elastic and elastoplastic calculations at σ_d^{-1} = 222.5 MPa.

is shown figure 24. The $\langle FIP_{cr}\rangle_{p=0.5}$ of machined specimens is calculated from the experimental SN-curve data. The stress field within the machined specimens is supposed to be homegeneous so that the $\langle FIP_{cr}\rangle_{p=0.5}$ is directly proportional to the applied stress. For as-built specimens, the $\langle FIP_{cr}\rangle_{p=0.5}$ is calculated by applying the nominal maximum stress corresponding to the nominal maximum stress applied during HCF testings. The criticity of the stress field regarding the HCF behavior is slightly underestimated at 2×10^6 cycles. This is due to the profilometric analysis which is unable to capture the defect complexity in some cases and the numerous filtering steps used to build meshes suitable for computations. Since the Crossland parameters and the critical distance have been calculated for 2×10^6 cycles, this methodology is mostly valid for this number of cycles. The difference between elastic and elastoplastic computations is noticeable when the applied mean stress is sufficiently high. Figure 23-b shows the result of the methodology for SVE built from tomographic analysis. The simulations give a good estimation of the criticity of the stress field regarding HCF behavior at 2×10^6 cycles. However, for higher applied mean stresses, the notch effect is overestimated. Two main reasons can explain this behavior: the plasticity is not well taken into account. Indeed, the plastic zone being obviously very local, an approach using crystal plasticity calculations should give better evaluation of the stress field at the notch tip. Current development aims at adressing this issue which is however outside the scope of this paper. The other reason could be the critical distance which has been calibrated from 2d calculations at 2×10^6 cycles and for an applied nominal maximum stress σ_d^{-1} = 222.5 MPa. The use of a critical distance is valid for a given number of cycles [40] and is one way to account for a defect sensitivity defined as: $q = \frac{K_f-1}{K_t-1}$ where $K_f = \frac{smooth\ \sigma_d}{notch\ \sigma_d}$. For a given material and a given defect it

is generally observed that the lower the number of cycles, the lower the difference between *smooth* σ_d and *notch* σ_d and so the lower q, meaning that at low number of cycles the critical distance should be bigger than at high number of cycles. When comparing the predictions for profilometric and tomographic data, an offset of approximately 35 MPa at 2×10^6 cycles appears between the two data sets which comes from the different descriptions of the surfaces.

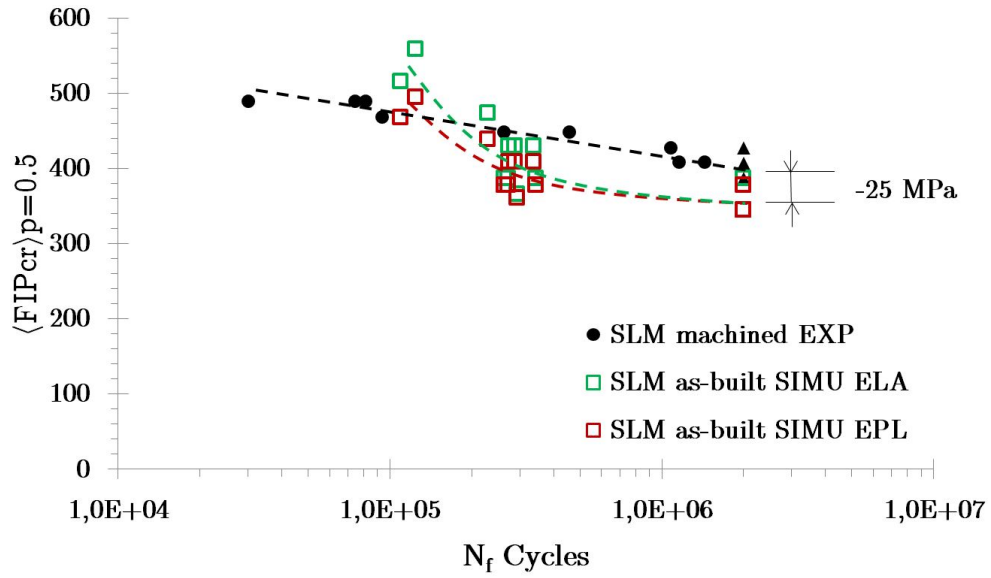

(a)

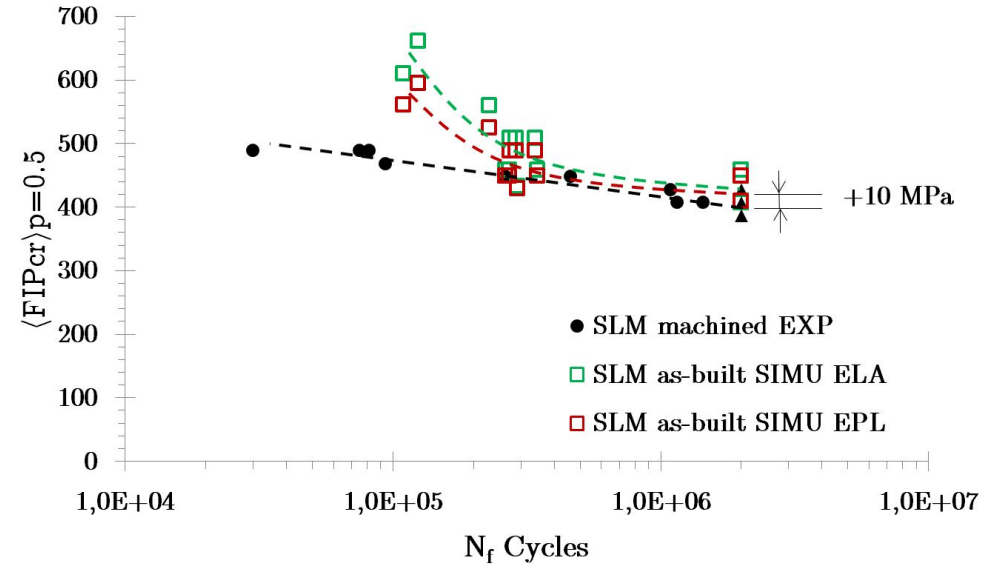

(b)

Fig. 23. Master Curve build for SVE obtained from profilometric analysis (a) and tomographic analysis (b).

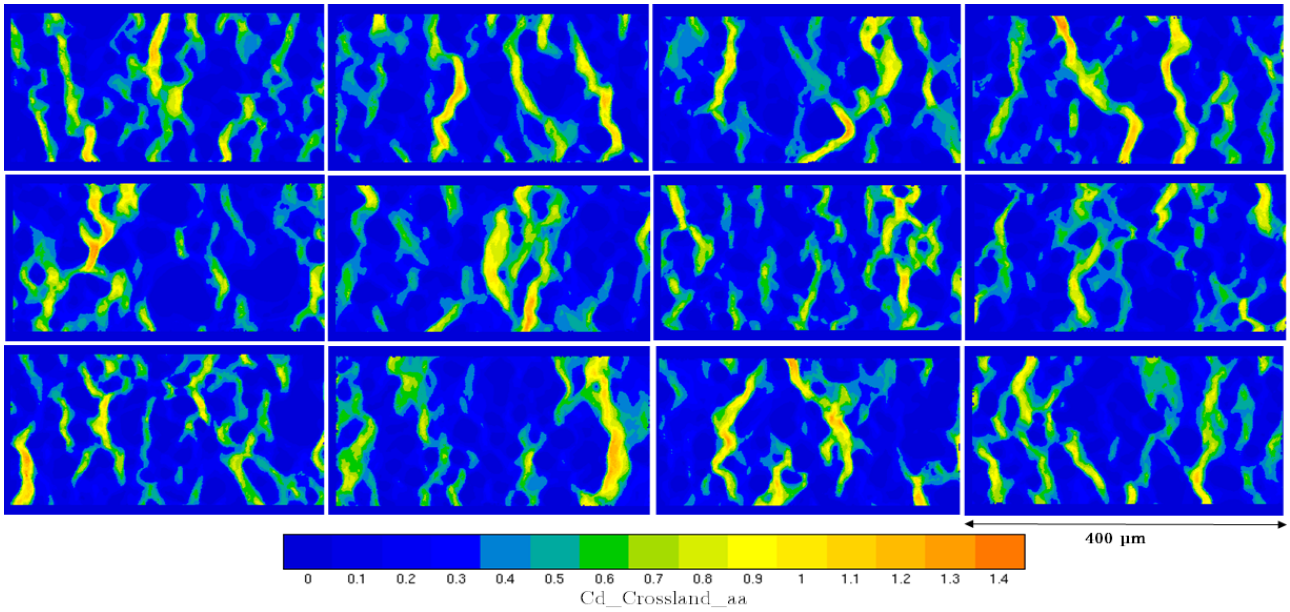

Fig. 24. Distribution of $\langle FIP_{cr} \rangle$ within SVE obtained from profilometric analysis.

4. Conclusion

In this study, a methodology accounting for the effect of the surface roughness on HCF strength of Ti-6Al-4V parts obtained by SLM has been developped. The procedure allows estimating the fatigue strength of as-built specimens from which the surface topology has been measured. The differences between elastic and elastoplastic computations regarding the non-local FIP values are very small (at 2×10^6 cycles), which indicates that the methodology is not much sensitive to the hardening law. However, a precise and representative description of the surface is needed in order to correctly take into account the notch effect and to consider a sufficent number of micronotches. The methodology highlighted the fact that measurements from profilometric analysis may not be suitable to predict the fatigue strength of parts obtained by SLM since the micronotches are not well described. One would prefer tomographic or micrographic measurements, which are able to reproduice faithfully the micronotch morphology associated to the surface. Computations taking into account the residual stresses should extend the validity of the methodology, which should also be challenged for multiaxial loadings. Considering the mechanical behavior as isotropic and homogeneous has to be seen as the first statistical momentum of the material behavior. In that sense, the use of an homogeneous behavior is sufficient in a first approximation, even if it will be limitated in terms of local mechanical field description. The authors are working on the use of cristal plasticity to evaluate more precisely the impact of local microstructures on the local stress strain state.

References

[1] D. K. Do, P. Li, The effect of laser energy input on the microstructure, physical and mechanical properties of Ti-6Al-4V alloys by selective laser melting, Virtual and Physical Prototyping 11 (1) (2016) 41–47.

[2] D. Gu, Y. C. Hagedorn, W. Meiners, G. Meng, R. J. S. Batista, K. Wissenbach, R. Poprawe, Densification behavior, microstructure evolution, and wear performance of selective laser melting processed commercially pure titanium, Acta Materialia 60 (9) (2012) 3849–3860.

[3] B. Song, S. Dong, B. Zhang, H. Liao, C. Coddet, Effects of processing parameters on microstructure and mechanical property of selective laser melted Ti6Al4V, Materials and Design 35 (2012) 120–125.

[4] P. Li, D. H. Warner, A. Fatemi, N. Phan, Critical assessment of the fatigue performance of additively manufactured Ti-6Al-4V and perspective for future research, International Journal of Fatigue 85 (2016) 130–143.

[5] P. Edwards, M. Ramulu, Fatigue performance evaluation of selective laser melted Ti-6Al-4V, Materials Science and Engineering A 598 (2014) 327–337.

[6] S. Leuders, M. Thöne, A. Riemer, T. Niendorf, T. Tröster, H. A. Richard, H. J. Maier, On the mechanical behaviour of titanium alloy TiAl6V4 manufactured by selective laser melting: Fatigue resistance and crack growth performance, International Journal of Fatigue 48 (2013) 300–307.

[7] G. Webster, A. Ezeilo, Residual stress distributions and their influence on fatigue lifetimes, International Journal of Fatigue 23, Supple (2001) 375–383.

[8] M. N. James, D. J. Hughes, Z. Chen, H. Lombard, D. G. Hattingh, D. Asquith, J. R. Yates, P. J. Webster, Residual stresses and fatigue performance, Engineering Failure Analysis 14 (2) (2007) 384–395.

[9] B. Van Hooreweder, R. Boonen, D. Moens, P. Sas, On the Determination of Fatigue Properties of Ti6Al4V Produced by Selective Laser Melting On the determination of fatigue properties of Ti6Al4V produced by selective laser melting (April 2012).

[10] H. Gong, K. Rafi, H. Gu, G. D. Janaki Ram, T. Starr, B. Stucker, Influence of defects on mechanical properties of Ti-6Al-4V components produced by selective laser melting and electron beam melting, Materials and Design 86 (2015) 545–554.

[11] H. K. Rafi, N. V. Karthik, H. Gong, T. L. Starr, B. E. Stucker, Microstructures and Mechanical Properties of Ti6Al4V Parts Fabricated by Selective Laser Melting and Electron Beam Melting 22 (December) (2013) 3872–3883.

[12] H. Atkinson, S. Davies, Fundamental aspects of hot isostatic pressing: an overview, Metallurgical and Materials Transactions A 31A (December) (2000) 2981–3000.

[13] H. Neuber, Theory of Stress Concentration for Shear-Strained Prismatical Bodies With Arbitrary Nonlinear Stress-Strain Law, Journal of Applied Mechanics 28 (4) (1961) 544.

[14] D. Arola, M. Ramulu, An Examination of the Effects from Surface Texture on the Strength of Fiber Reinforced Plastics, Journal of Composite Materials 33 (2) (1999) 102–123.

[15] D. Arola, C. L. Williams, Estimating the fatigue stress concentration factor of machined surfaces, International Journal of Fatigue 24 (9) (2002) 923–930.

[16] Peterson, Peterson's Stress Concentration Factors, 1974.

[17] S. As, B. Skallerud, B. Tveiten, Surface roughness characterization for fatigue life predictions using finite element analysis, International Journal of Fatigue 30 (2008) 2200–2209.

[18] V. N. E. Frost, K. J. Marsh, L. P. Pook, Metal fatigue., Materialwissenschaft und Werkstofftechnik.

[19] R. A. Smith, K. J. Miller, Prediction of fatigue regimes in notched components, International Journal of Mechanical Sciences 20 (4) (1978) 201–206.

[20] T. Palin-Luc, S. Lasserre, J. Y. Berard, Experimental investigation on the significance of the conventional endurance limit of a spheroidal graphite cast iron, Fatigue and Fracture of Engineering Materials and Structures 21 (2) (1998) 191–200.

[21] M. H. El Haddad, T. H. Topper, K. N. Smith, Prediction of non propagating cracks, Engineering Fracture Mechanics 11 (3) (1979) 573–584.

[22] Y. Murakami, T. Endo, Effects of small defects on fatigue strength of metals, International Journal of Fatigue 2 (1) (1980) 23–30.

[23] Y. Murakami, M. Endo, Effects of defects, inclusions and inhomogeneities on fatigue strength, International Journal of Fatigue 16 (3) (1994) 163–182.

[24] Y. Murakami, Chapter 4 - Effect of Size and Geometry of Small Defects on the Fatigue Limit, in: Metal Fatigue, 2002, pp. 35–55.

[25] D. Taylor, Geometrical effects in fatigue: a unifying theoretical model, International Journal of Fatigue 21 (5) (2000) 413–420.

[26] D. Taylor, Prediction of fatigue failure location on a component using a critical distance method 22 (2000) 735–742.

[27] Y. Nadot, T. Billaudeau, Multiaxial fatigue limit criterion for defective materials, Engineering Fracture Mechanics 73 (1) (2006) 112–133.

[28] F. Morel, N. Huyen, Plasticity and damage heterogeneity in fatigue 49 (2008) 98–127.

[29] C. P. Przybyla, D. L. Mcdowell, Simulated microstructure-sensitive extreme value probabilities for high cycle fatigue of duplex Ti 6Al 4V, International Journal of Plasticity 27 (12) (2011) 1871–1895.

[30] A. Hor, N. Saintier, C. Robert, T. Palin-Luc, F. Morel, Statistical assessment of multiaxial HCF criteria at the grain scale, International Journal of Fatigue 67 (2014) 151–158.

[31] Gmsh: a three-dimensional finite element mesh generator with built-in pre-and post-processing facilities, International Journal for Numerical Methods in Engineering 79(11) 0 (2009) 1309–1331.

[32] C. O. Frederick, P. J. Armstrong, A mathematical representation of the multiaxial Bauschinger effect, Materials at High Temperatures 24 (1) (2007) 1–26.

[33] B. Crossland, Effect of large hydrostatic pressures on the torsional fatigue strength of an alloy steel (1956) 12.

[34] M. El May, N. Saintier, T. Palin-Luc, O. Devos, Non-local high cycle fatigue strength criterion for metallic materials with corrosion defects, Fatigue and Fracture of Engineering Materials and Structures 38 (9) (2015) 1017–1025.

[35] H. Dehmani, C. Brugger, T. Palin-Luc, C. Mareau, S. Koechlin, High cycle fatigue strength assessment methodology considering punching effects, Procedia Engineering 213 (2017) (2018) 691–698.

[36] G. Lütjering, J. C. Williams, Titanium, 2nd Edition, Springer, 2007.

[37] Y. Matsumoto, F. Hashimoto, G. Lahoti, Surface Integrity Generated by Precision Hard Turning, CIRP Annals - Manufacturing Technology 48 (1) (1999) 59–62.

[38] G. Kasperovich, J. Hausmann, Improvement of fatigue resistance and ductility of TiAl6V4 processed by selective laser melting, Journal of Materials Processing Technology 220 (2015) 202–214.

[39] V. Chastand, A. Tezenas, Y. Cadoret, P. Quaegebeur, W. Maia, E. Charkaluk, Fatigue characterization of Titanium Ti-6Al-4V samples produced by Additive Manufacturing, Procedia Structural Integrity 2 (2016) 3168–3176.

[40] Y. Yamashita, Y. Ueda, H. Kuroki, M. Shinozaki, Fatigue life prediction of small notched Ti-6Al-4V specimens using critical distance, Engineering Fracture Mechanics 77 (9) (2010) 1439–1453.